



Lizards exploit the changing optics of developing chromatophore cells to switch defensive colors during ontogeny

Gan Zhang^{a,1} , Venkata Jayasurya Yallapragada^{b,c} , Topaz Halperin^{d,e} , Avital Wagner^a , Michal Shemesh^d , Alexander Upcher^f , Iddo Pinkas^g , Harry L. O. McClelland^h , Dror Hawlena^{d,2} , and Benjamin A. Palmer^{a,2}

Edited by Joanna Aizenberg, Harvard University, Cambridge, MA; received September 7, 2022; accepted March 16, 2023

Many animals undergo changes in functional colors during development, requiring the replacement of integument or pigment cells. A classic example of defensive color switching is found in hatchling lizards, which use conspicuous tail colors to deflect predator attacks away from vital organs. These tail colors usually fade to concealing colors during ontogeny. Here, we show that the ontogenetic blue-to-brown tail color change in *Acanthodactylus beershebensis* lizards results from the changing optical properties of single types of developing chromatophore cells. The blue tail colors of hatchlings are produced by incoherent scattering from premature guanine crystals in underdeveloped iridophore cells. Cryptic tail colors emerge during chromatophore maturation upon reorganization of the guanine crystals into a multilayer reflector concomitantly with pigment deposition in the xanthophores. Ontogenetic changes in adaptive colors can thus arise not via the exchange of different optical systems, but by harnessing the timing of natural chromatophore development. The incoherent scattering blue color here differs from the multilayer interference mechanism used in other blue-tailed lizards, indicating that a similar trait can be generated in at least two ways. This supports a phylogenetic analysis showing that conspicuous tail colors are prevalent in lizards and that they evolved convergently. Our results provide an explanation for why certain lizards lose their defensive colors during ontogeny and yield a hypothesis for the evolution of transiently functional adaptive colors.

guanine | lizard | development | ontogenetic color | chromatophore

Many animals undergo progressive changes in color during development (ontogenetic color change) driven by variations in environment such as predation risk (1–7). These adaptive color changes are typically achieved via the replacement of integument (e.g., feathers, pelt) or the production of new pigment cells (1, 8, 9). Changes in predation risk induce spectacular switches in defensive colors from masquerade to aposematic (10) or from cryptic to less cryptic (11). A classic example of defensive color switching is found in many lizards, which, as hatchlings use colorful, autotomizable tails to redirect predator attacks away from the vital organs to increase survival probability (12–19). These conspicuous tail colors usually fade during ontogeny, sometimes only weeks after hatching (12, 20). Little is known about why lizards lose this profitable defense mechanism or the optical mechanisms underlying the color change. Answering these questions can provide insights on the formation of the component photonic structures and the evolution of transiently functional adaptive colors.

Here, we quantify the evolutionary history of the conspicuous tail color phenomenon in lizards, showing that it is a highly prevalent trait that convergently evolved. We show that the ontogenetic blue-to-brown color change in the Be'er Sheva fringe-fingered lizard (*Acanthodactylus beershebensis*) results from the changing optical properties of single types of iridophore and xanthophore cells as they form. The matte blue tail color of hatchling lizards is produced by incoherent scattering from disordered assemblies of premature guanine crystals in underdeveloped iridophore cells. Light brown adult tail colors emerge during chromatophore maturation, upon orientational ordering of the guanine crystals in the iridophores, concomitantly with xanthophore pigmentation. Ontogenetic changes in adaptive colors can thus arise not by the substitution of pigment cells or integument, but by harnessing the timing of chromatophore development to exploit different optical phenomena which emerge during cell formation.

The incoherent scattering mechanism underlying the blue color here has not been documented in guanine systems before (21, 22) and differs from the multilayer interference mechanism used in other blue-tailed lizards (23, 24). The ability to generate a similar trait from different optical mechanisms agrees with our ancestral state reconstruction, which suggests that conspicuous tail colors in lizards convergently evolved. Ultimately, our results provide an explanation for why lizards lose this beneficial trait during ontogeny, yielding

Significance

Studying functional color changes during animal development provides a means of understanding the evolution and formation of animal color. Here, we find that blue-to-brown changes in defensive colors in certain developing lizards occurs not by the energetically costly exchange of different optical systems but by exploiting the changing optics of single types of maturing pigment cells. The optical mechanism involves the transformation of a disordered guanine scatterer into a multilayer reflector coupled with pigmentation of the developing xanthophores. These results reveal a way for generating blue color from guanine crystals via incoherent scattering rather than multilayer interference. The results provide insights on the assembly of guanine photonic superstructures and the evolution of conspicuous tail colors in lizards.

Author contributions: G.Z., D.H., and B.A.P. designed research; G.Z., V.J.Y., T.H., A.W., M.S., A.U., I.P., D.H., and B.A.P. performed research; V.J.Y. contributed new reagents/analytic tools; G.Z., V.J.Y., T.H., and A.W. analyzed data; and G.Z., V.J.Y., A.W., H.L.O.M., D.H., and B.A.P. wrote the paper.

The authors declare no competing interest.

This article is a PNAS Direct Submission.

Copyright © 2023 the Author(s). Published by PNAS. This open access article is distributed under Creative Commons Attribution-NonCommercial-NoDerivatives License 4.0 (CC BY-NC-ND).

¹Present address: College of Chemistry and Chemical Engineering, Lanzhou University, Lanzhou 730000, China.

²To whom correspondence may be addressed. Email: dror.hawlena@mail.huji.ac.il or bpalmer@bgu.ac.il.

This article contains supporting information online at <https://www.pnas.org/lookup/suppl/doi:10.1073/pnas.2215193120/-DCSupplemental>.

Published April 27, 2023.

an evolutionary hypothesis to explain the relationship between colorful tails and risk-taking behaviors in lizards.

Results

A literature review of 7,310 classified species revealed that 361 lizard species possess colorful tails (215 blue and 146 red), at one stage of their lifetime (*SI Appendix, Tables S1 and S2*). Of these, 146 species go through an ontogenetic change from colorful to cryptic tails, but only two species go through a reverse ontogenetic change (cryptic to colorful). We estimate that 63% of Lacertidae and 30% of Teiidae and Scincidae species undergo ontogenetic changes in tail color. Stochastic character mappings show that tail coloration is a flexible evolutionary trait (Fig. 1 and *SI Appendix, Table S3*), revealing 127 changes between tail coloration categories. Blue tails were gained 28.4 times and lost 62.7 times and red tails were gained 39.2 times and lost 18.9 times (*SI Appendix, Table S3*).

Maximum parsimony reconstruction revealed 73 evolutionary transitions between tail colors, with blue tails gained 21 times and lost 43 times and red tails gained 26 times and lost 5 times (*SI Appendix, Table S3*). Some transitions occurred in late evolutionary history during the most recent speciation events (Fig. 1A). In the genus *Acanthodactylus* in Lacertidae, most species possess colorful tails as juveniles (at least 23 species out of 34), and at least 80% of these also lose it in adulthood. With very high probability, the ancestral tail color of *Acanthodactylus* was blue (Fig. 1B). Since ontogenetic color changes are particularly prevalent in *Acanthodactylus*, we were motivated to explore the optical mechanisms underlying tail color changes in a model species—*A. beershebensis*. Moreover, the nonsaturated, matte blue tail color in this clade is different from the saturated, bright blue tail of the previously investigated skink, *Plestiodon latiscutatus* (produced by multilayer interference) (23, 24), indicating that a different optical mechanism could be found in this case.

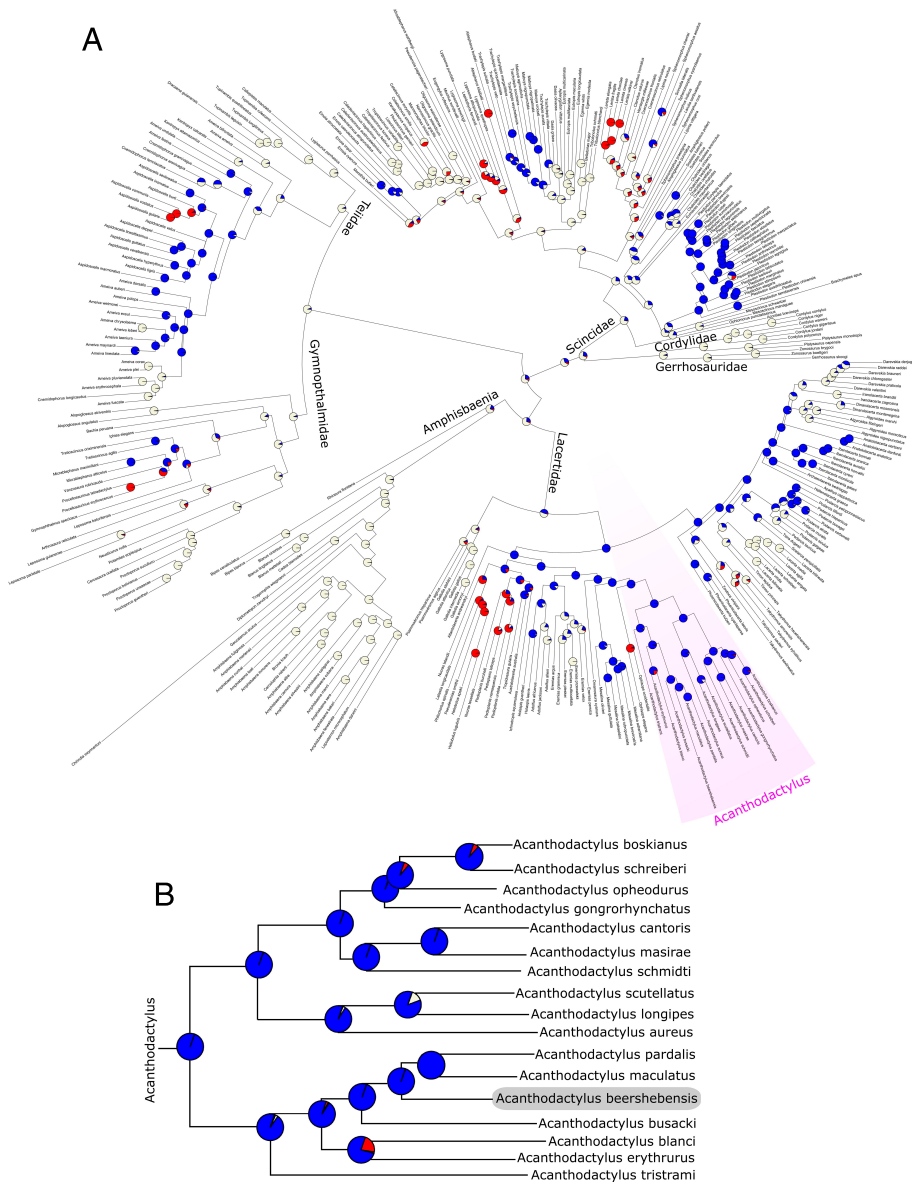


Fig. 1. Ancestral state reconstruction of colorful tails using stochastic character mapping. Pies in the nodes show the posterior probabilities for their character state reconstructed in stochastic character mapping simulations. Colors: blue; blue tail coloration; red; red tail coloration; beige; cryptic tail coloration. Note that some sister species belong to different tail color categories (e.g., Lacertidae: *Acanthodactylus longipes* and *A. scutellatus*; Scincidae: *Plestiodon reynoldsi* and *P. egregius*; Teiidae: *Ameiva wetmorei* and *A. exsul*). The *Acanthodactylus* genus is pseudo-colored in pink. (A) Lacertidae and Scincomorpha. (B) The reconstructed phylogenetic tree of *Acanthodactylus* extracted from A.

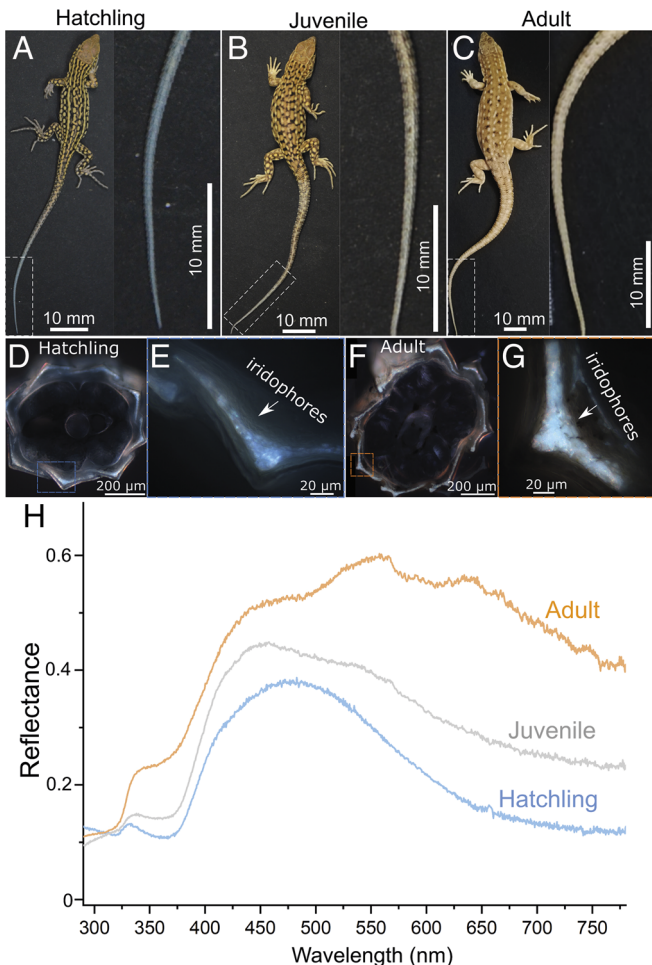


Fig. 2. Optical properties of *A. beershebensis* tails during ontogeny. (A–C) Dorsal-lateral views of hatchling, juvenile, and adult *A. beershebensis* and the corresponding high-magnification views of the tails. (D–G) Polarizing optical micrographs of cross-sections of the hatchling tail (D and E) and the adult tail (F and G). (H) Reflectance spectra from posterior regions of the tails in different developmental stages. The total reflectance increases with development. All spectra exhibit a small peak in the UV at ~330 nm and a sharp drop in reflectance intensity from ~420 to 375 nm.

To explore the optical and physical mechanisms underlying these ontogenetic changes in tail color, we followed color changes in *A. beershebensis* lizards during ontogeny. The lizards hatch with a conspicuous, matte blue tail, whose reflectance spectrum exhibits a single broad peak at ~460 nm (Fig. 2 A and H). Within 2 wk, the blue tail color fades to a whitish-gray color, and a small peak at ~550 nm emerges—broadening the reflectivity spectrum (Fig. 2 B and H). Approximately 4 wk after hatching, the tail color transforms into a cryptic light brown (Fig. 2 C) exhibiting broad reflectance, with minor peaks at ~550 nm and ~630 nm (Fig. 2 H). Polarizing optical micrographs of cross-sections through hatchling (Fig. 2 D and E) and adult tails (Fig. 2 F and G) reveal highly birefringent, dermal iridophores, which, in adults, are interspersed with xanthophores.

Skin color in lizards is produced by layers of different pigment cells, collectively termed—the dermal chromatophore unit (25). To elucidate the mechanism underlying this color change, we imaged the ultrastructure of the component chromatophore cells during ontogeny. In reptile skin, the uppermost xanthophores contain pteridine and carotenoid pigments and function as spectral filters (26–29). The underlying iridophores produce reflective colors due to the high refractive index and nanostructural organization of the component guanine crystals (22, 30–33). Light

transmitted through the guanine layer is absorbed by the lowest melanophore layer (25, 27). In contrast to this “textbook” view of the dermal chromatophore unit in lizards (23, 31, 34), the melanophores in *A. beershebensis* are extremely sparsely distributed in all developmental stages (*SI Appendix*, Figs. S1, S2, and S4). Since there is also no significant change in the distribution of the sparsely populated melanophores during ontogeny, their contribution to the color change in these lizards is minimal. Transmission electron microscopy (TEM) (Fig. 3 A and B and *SI Appendix*, Fig. S3 A–C) reveals that hatchling xanthophores contain empty pigment granules (pterinosomes) (35), free from electron-dense pigment and exhibiting round intraluminal inclusions and membrane invaginations (Fig. 3B, black arrow). All of these features are characteristic of premature pterinosome organelles (36). After 4 to 7 wk (Fig. 3D), pigment condenses inside the pterinosomes, which develop an onion-like lamellae structure (Fig. 3 E and F, red arrow, *SI Appendix*, Fig. S3 D–F)—characteristic of mature pterinosomes (36, 37). In both hatchlings and adults, the iridophores contain angular void spaces—indicative of guanine crystals lost during sample preparation for TEM (Fig. 3 C and E) (38–40). The number of iridophore layers in a transverse section of the dermis increases from 2 in hatchlings to 4 or 5 in adults.

While the maturation of the xanthophore pigment organelles during development can be clearly seen in TEM, guanine crystals are lost during tissue preparation (40). We thus used cryogenic-scanning electron microscopy (cryo-SEM) to image the xanthophores and iridophores at different development stages. Cryo-SEM enables the guanine crystals to be imaged in their native, hydrated state (Fig. 4 and *SI Appendix*, Figs. S4 and S5). Hatchling iridophores contained randomly oriented, membrane-bound, ellipsoidal vesicles (Fig. 4A) and a few faceted crystals. Fractures through these vesicles reveal minute, partially formed guanine crystals (Fig. 4B and *SI Appendix*, Fig. S6) constructed from separate nanoscopic platelets (platelet thickness: ~12 nm) and surrounded by aqueous material (38, 39, 41). Vesicles containing the smallest crystals had a circular cross-section (Fig. 4C, blue arrow). More mature crystals extend across the width of the vesicle, causing the membrane to reshape around the growing crystal, adopting its morphology (i.e., an oval cross-section, Fig. 4C, red arrow, *SI Appendix*, Fig. S6). Similarly, hatchling xanthophores are also underdeveloped (Fig. 4 D and E). Pterinosome granules are filled by smoothly textured, aqueous material and often exhibit membrane invaginations as observed in TEM (Fig. 4D, cyan arrow, Fig. 3B, black arrow), indicating that the xanthosomes are not yet pigmented. Cryo-SEM images of juveniles (~2 wk post-hatching) show the next stage of chromatophore maturation. More faceted vesicles are observed in the iridophores as the membranes condense around the surface of the forming crystals (Fig. 4F). At this transitional stage of ontogeny, the crystals, though still positionally disordered, begin to exhibit a preferred orientation. The distinctly separated platelets of the immature hatchling crystals have coalesced to form single, coherent crystals (Fig. 4 G and H and *SI Appendix*, Fig. S6) which are determined as the β-guanine crystalline phase (*SI Appendix*, Figs. S7 and S8) (42, 43). This coalescence of crystal platelets was also observed in guanine formation in other organisms and appears to be a fundamental feature of guanine biocrystallization (41, 44, 45). This allows us to use crystal texture as a measure for the developmental state of the iridophore cells. The pterinosome granules in the juvenile xanthophores exhibit a more fibrous character (Fig. 4 I and J), but have not yet developed the characteristic “onion-like” texture associated with mature, pigmented xanthosomes (36). In the adult, the iridophores are larger than in the hatchling and juveniles and are filled with mature, irregular polygonal crystals (mean size ~ 500 × 270 ×

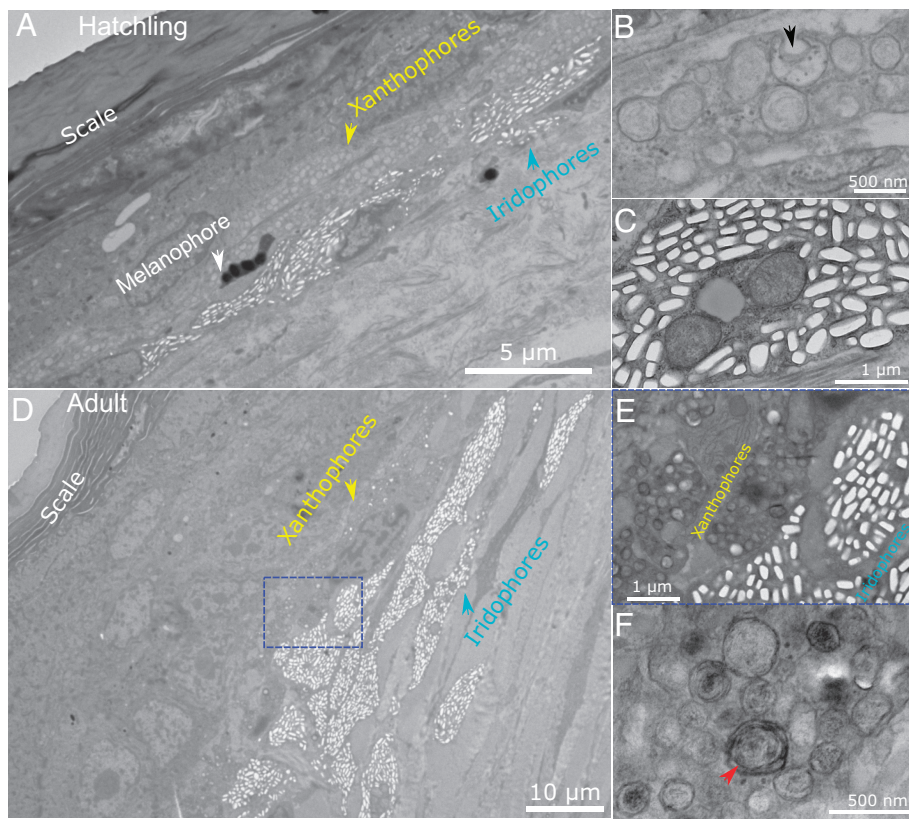


Fig. 3. TEM micrographs of cross-sections through hatchling and adult tails. (A) Low-magnification TEM image of a hatchling tail. (B and C) High-magnification TEM images of hatchling xanthophores and iridophores. (D) Low-magnification TEM image of an adult tail. (E and F) High-magnification TEM images of adult xanthophores and iridophores. We estimate that the hatchling lizards were between 5 and 10 d post-hatching, and the adult lizards (with the light brown tail color) were between 5 and 8 wk post-hatching.

85 nm³). Few ellipsoidal vesicles are observed. The crystals are arranged into stacks separated by cytoplasm, exhibiting some disorder in crystal orientation and spacing between crystals—a disordered multilayer reflector (Fig. 4K). Each multilayer domain occupies an area of approximately 3 × 3 μm². Individual domains in a single iridophore are misoriented with respect to one another (Fig. 4 K–M). Pigment granules in the xanthophores exhibit an onion-like structure reminiscent of mature, pigmented pterinosomes (Fig. 4 N and O) (36).

To quantify changes in the orientational ordering of the guanine crystals in the hatchling, juvenile, and adult iridophores, we performed fast Fourier transform (FFT) analysis on cryo-SEM images from all states (Fig. 5, *SI Appendix*, Fig. S9, and *Materials and Methods*). Directionality analysis (46, 47) (*SI Appendix*, Fig. S9) and entropy calculations (*SI Appendix*, Datasets S1–S4) (48) were performed on 39 cryo-SEM images (13 from each developmental state). These analyses showed that there is a lack of orientational ordering of the crystals in hatchling iridophores (Fig. 5). Average entropies of 2.71 ± 0.11, 2.59 ± 0.21, and 2.15 ± 0.38 were found for the orientation histogram of hatchling, juvenile, and adult lizards, respectively. An unpaired *t* test showed that there is high statistical significance (>95%) to these entropy values, confirming that the crystals in adult lizard iridophores have a higher degree of orientational ordering than that in juveniles and hatchlings. This gradual transition from disorder to order of crystal orientations during the maturation agrees with a visual inspection of the cryo-SEM images (Fig. 5 A, C, and E). Conversely, the presence of orientational ordering of the crystals in adult iridophores is consistent with disordered multilayer stacks (Fig. 5 E and F).

Our microscopy analysis shows that the melanophores are sparsely populated in *A. beershebensis* across all developmental stages

(Fig. 3 and *SI Appendix*, Figs. S1, S2, and S4). Thus, the blue-to-brown color change during ontogeny must be dictated by changes in the optical properties of the iridophores and xanthophores. In hatchlings and juveniles, the xanthophores are unpigmented (Fig. 3 and *SI Appendix*, Fig. S4); therefore, the tail coloration in these stages is determined only by the iridophores. Conversely, adult colors will be determined by the combined optical response of the iridophores and the overlying, pigmented xanthophores.

Based on the crystal size and organization obtained from cryo-SEM (Figs. 4 and 5 and *SI Appendix*, Figs. S4, S5, and S9), we performed electromagnetic calculations to rationalize how the optical properties of the iridophore cells change during ontogeny. In hatchlings, long-range orientational and positional ordering between crystals is absent (Fig. 5 A and B). Therefore, we expect the scattering response of individual particles to contribute significantly to the color of the assemblies. Finite-difference time-domain (FDTD) calculations (Fig. 6A) (49, 50) showed that the total scattering cross-sections exhibit greater scattering in the blue region of the spectrum, which can account for the blue color of the hatchling tail. However, in contrast to these calculated spectra, the measured reflectance does not increase monotonically as the wavelength decreases but exhibits a peak at ca. 470 nm and a significant drop at smaller wavelengths. Short-range structural correlations of the guanine crystals (e.g., local stacking), absorption by soft tissue (e.g., collagen) (51) or melanin (52) could be responsible for the decreased reflectance at short wavelengths resulting in the appearance of the peak at 470 nm.

In the juvenile state, the tails appear grayish-white with a higher brightness (Fig. 2 A, B, and H) than the hatchling tail. Since the xanthophores are not yet fully pigmented in this state, the grayish-white color must be produced by broadband

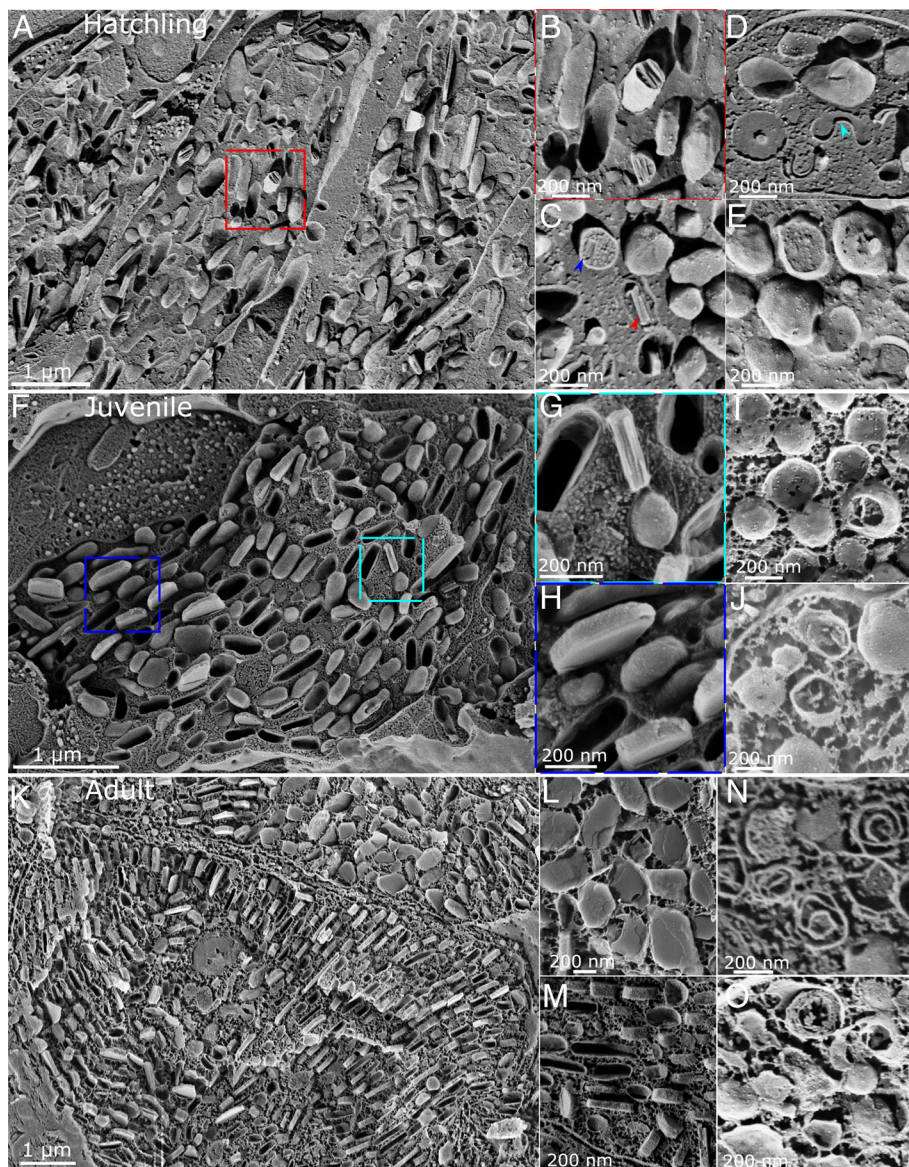


Fig. 4. Cryo-SEM micrographs of the chromatophores during ontogeny. (A) Clusters of iridophores in a hatchling tail. (B and C) High-magnification images of the crystal vesicles in the iridophores. Minute, partially formed crystals composed of nanoscopic crystal layers are observed in the fractured vesicles (C is taken from a different region of the sample). (D and E) High-magnification images of fractured pigment granules in the hatchling xanthophores. (F) A single iridophore in the juvenile stage. (G and H) High-magnification images of guanine crystals from the same iridophore. (I and J) High-magnification images of pterinosome vesicles containing fibrous structures in juvenile xanthophores. (K) Iridophores in an adult tail packed with mature guanine crystals. (L and M) High-magnification images of the mature guanine crystals oriented in different directions. (N and O) Mature pterinosomes with concentric lamellar structures in the adult xanthophores. We estimate that the hatchling lizards were between 3 and 5 d post-hatching, the juvenile lizards were between 2 and 3 wk post-hatching, and the adult phenotype lizards were between 4 and 6 wk post-hatching.

reflectance from disorganized guanine crystals in the iridophores. The guanine crystals in the iridophores of the adult are larger than those in the hatchling and juvenile (~ 500 nm long and 85 ± 25 nm thick) and are organized into disordered multilayer domains, which are misoriented with respect to one another. We modeled the optical properties of such a structure as a multilayer reflector using the average crystal thickness (81 nm) and cytoplasm spacing (88 nm) observed in cryo-SEM. A perfectly ordered multilayer with the given thickness and spacing would exhibit a high reflectance plateau centered at ~ 550 nm—a typical signature of a photonic bandgap (SI Appendix, Fig. S10A, deep blue trace) (53). However, the cryo-SEM observation shows that the iridophores contain numerous misoriented multilayer domains, and each domain exhibits significant disorder in crystal thickness and spacing. To account for this disorder, we introduced variations in the incident angle together with random deviations from mean

values of crystal thickness and cytoplasm spacing into the calculations. The calculated reflectance is significantly broadened (Fig. 6B) upon introducing disorder into the system. Indeed, even small deviations in crystal thickness, spacing, and number of crystal layers are sufficient to broaden the reflectance band (SI Appendix, Fig. S10 A and B), resulting in reflection throughout the visible spectrum. The light brown color of the adult tail is thus the resultant of reflectance from mature iridophores coupled with the absorption from overlying yellow/brown mature xanthophore layer.

Our models account for the major qualitative features of the spectra at visible wavelengths leading to coloration that arises from the organization of guanine crystals in iridophores and pigment deposition in xanthophores. The steep drop below 420 nm and the small peak at 330 nm, which are present at all stages of iridophore development, do not scale as expected with the size or organization

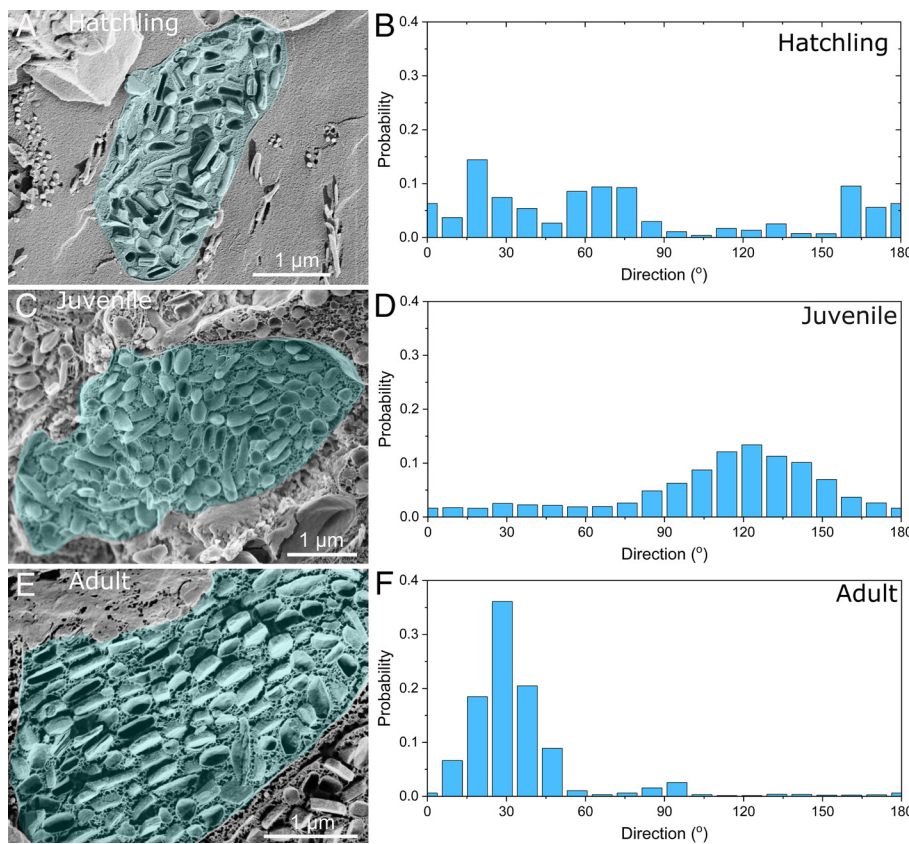


Fig. 5. Variation of the long-range orientational ordering of the guanine crystals from hatchling to adult iridophores. (A) Representative cryo-SEM image of the hatchling iridophore and (B) the histograms obtained from FFT analysis on the corresponding pseudo-colored (cyan) iridophore. (C) Representative cryo-SEM image of the juvenile iridophore and (D) the histograms obtained from FFT analysis on the corresponding pseudo-colored (cyan) iridophore. (E) Representative cryo-SEM image of the adult iridophore and (F) the histogram obtained from FFT analysis on the corresponding pseudo-colored (cyan) iridophore. The x axis in the histogram represents the directions of the crystals and the y axis represents the percentages of crystals in the specific direction.

of the guanine crystals, suggesting that they have a different origin (e.g., from absorption from the surrounding tissue) (51).

Discussion

Elucidating the ontogenetic color change mechanism in *A. beershebensis* yielded a previously unknown optical mechanism for producing blue color from guanine and showed that functional colors in animals can occur by exploiting the timing of natural chromatophore cell development.

Previous studies of biogenic guanine were focused on crystallization mechanisms (41, 44, 45, 54) or its optical functions in adult organisms (22, 55). However, this study provides insights on the assembly of guanine photonic superstructures. The blue-to-brown tail color change of *A. beershebensis* involves the transformation of a guanine scatterer into a multilayer reflector via gradual orientational ordering of crystals (Figs. 4 and 5). In scallop eyes, crystal orientation was found to be “preprogrammed” into the system prior to nucleation, ensuring that the crystals are coaligned in the mirror to generate a focal point on the retinae (45). In contrast, coorientation of the multilayers in adjacent iridophores is not required in adult lizards where the iridophores generate a broadband reflective layer under the xanthophores. The reorientational ordering of the guanine crystals during iridophore maturation is consistent with a nondirected assembly process where the increase in size and density of the plate-like crystals favors assembly into a multilayer superstructure. The constituent guanine crystals form by the coalescence of nanoscopic platelets (Fig. 4 and *SI Appendix*, Fig. S6) and, as growth proceeds, the

organelle membrane condenses on the surface of the crystal, adopting its morphology. Similar observations in spiders (41), fish (44), and scallops (45) suggest that these may be universal features of guanine bio-crystallization.

Unlike many other lizards which hatch with fully developed chromatophores (56–59), the blue color of *A. beershebensis* hatchlings arises from scattering by premature iridophores in the presence of unpigmented xanthophores. Light brown adult tail colors derive from absorption from the pigmented xanthophores coupled with multilayer reflection from the mature iridophores underlying them. Similar observations in *A. boskianus* and *A. scutellatus* (*SI Appendix*, Fig. S11) indicate that this color change mechanism may be common in this genus, and, perhaps in other matte blue-tailed lizards undergoing ontogenetic color change. Further evidence of a “delay” in chromatophore development is established by comparison with other species within *Acanthodactylus* which develop at a “normal” rate. *SI Appendix*, Fig. S12 shows that the iridophore and erythrophore cells in the red tail of the hatchling *A. schreiberi* are fully formed.

Canonically, ontogenetic color changes require the replacement of pigment cell types or the substitution of cuticle, pelt, and feathers (60). Instead, in *A. beershebensis*, the transformation from defensive blue colors to cryptic light-brown colors is generated by the same chromatophore cells at different maturation stages. Thus, transitional cell states can be exploited for specific adaptive optical functions upon maturation. While other animals undergo ontogenetic color change from the restructuring of exoskeleton or reorganization of single pigment cell types (61–64), the adaptive significance of these color change is generally not known. Our results provide an explanation to the long-standing discussion of

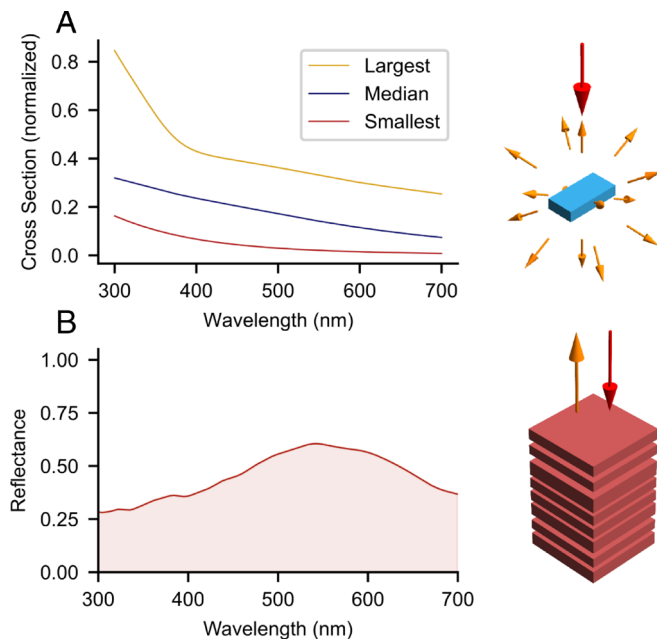


Fig. 6. Calculated scattering and reflectivity properties of the iridophores during development. (A) Calculated scattering spectra of single guanine crystals of various crystal sizes observed in hatching iridophores. The spectra exhibit higher scattering in the blue region of the spectrum. Blue trace: median crystal size ($325\text{ nm} \times 185\text{ nm} \times 50\text{ nm}$); red trace: smallest crystals ($150\text{ nm} \times 85\text{ nm} \times 35\text{ nm}$); yellow trace: largest crystals ($500\text{ nm} \times 270\text{ nm} \times 85\text{ nm}$). The spectra are the average for two orthogonal polarizations. (B) Calculated reflectance spectrum of multilayer stacks of guanine crystals as observed in adult iridophores. The spectrum is the average of 420 trials of eight layers of guanine crystals interspersed by cytoplasm (with constant crystal thickness at 81 nm and cytoplasm spacing at 88 nm , estimated from cryo-SEM data), incorporating a range of angles of incidence (from 0 to 20°) and disorder in crystal thicknesses and spacings (the value of the disorder is 30 nm , estimated from cryo-SEM data).

why some young lizards lose their effective defensive colors weeks after hatching (12). We hypothesize that natal dispersal, competition for limited resources, and potentially other ecological factors (e.g., prey size and availability) favor active foraging in hatchlings (65). Active foraging renders crypsis less effective and selects for alternative defensive strategies and coloration. Lizards with delayed chromatophore development may have a selective advantage because they hatch when the tail is still blue, which increases their probability of surviving inevitable attacks by predators. As the chromatophores develop and the blue color is lost, lizards must become less active to reduce detectability.

Many blue colors produced by guanine-based systems (21, 66), including lizard tails in other taxa, are generated by constructive interference from highly ordered multilayers (19, 23, 24), resulting in saturated colors (22). In contrast, the blue tail color of *A. beershebensis* hatchlings is produced by incoherent scattering, resulting in an unsaturated, matte blue. Our literature review and ancestral state reconstruction shows that many lizards hatch with blue tails that fade during development (12, 13, 16, 17, 20, 67) and that this trait was independently gained and lost many times (Fig. 1 and *SI Appendix, Table S3*). Our mechanistic results support this convergent evolutionary scenario since they show that at least two different optical mechanisms produce the conspicuous blue tail phenotype.

Materials and Methods

Literature Review and Evolutionary Reconstruction of the Blue Tail Phenomenon. We gathered relevant data on the tail colors of lizards from hundreds of books and scientific papers, published before 2014 to 2015 (*SI Appendix, Extended Methods*). We focused on the Lacertoidae and Scincoidae superfamilies

(68), which include six families that were known from previous studies to include lizards with colorful tails (69, 70). Ultimately, our data included 1,659 species on which adult tail coloration was known and 348 species on which juvenile coloration was known. Tail coloration was classified into three categories: i) cryptic tails, ii) conspicuous blue tails, and iii) conspicuous red tails. Tracing the phylogenetic history of tail coloration was based on juvenile tail coloration. Ancestral states were reconstructed using stochastic character mapping (71), implemented in the function *make.simmap* in the *phytools* package in R (72). To compare our phylogenetic history assessments with the most conservative approach, we conducted a parsimony analysis using the function *minCharChange* in *paleotree* package (73). The phylogenetic tree for the analysis was adopted from Pyron et al. (68). Since this tree encompasses the entire Squamata clade, it was truncated based on our database (i.e., species not included in the database were removed from the tree).

Specimen Collection and Preparation. All *A. beershebensis* (hatchling, juvenile, and adult) specimens were collected in the Loess Park Nature Reserve, Northern Negev, Israel (permit number 2020/42592). The live lizards were calmed in the refrigerator at $4\text{ }^\circ\text{C}$ for 10 min for optical microscopy and the reflectance measurements. The last 1 cm of the lizard tails was removed and fixed in 4% paraformaldehyde in $1 \times$ PBS fixative in the dark. The tails were fixed for more than 72 h and stored in a refrigerator at $4\text{ }^\circ\text{C}$ until analyzed further by optical microscopy, cryo-SEM, TEM and Raman spectroscopy. The fixed tails were placed in $1 \times$ PBS solution for 2 h and then embedded in 7% agarose gel ($1 \times$ PBS as the medium) and cut into $180\text{ }\mu\text{m}$ horizontal sections by a vibratome (LEICA VT1000S). All lizards were released at the exact location of capture in less than 4 h.

Optical Microscopy. The optical microscopy and polarized light microscopy imaging was performed on live samples and on fixed tissue sections cut with a vibratome. The samples were imaged using a Zeiss AX10 microscope equipped with a Zeiss AxioCam 705 color camera using reflection, transmission, or polarization mode with $5\times$, $10\times$, $20\times$, and $50\times$ air objectives.

Reflectance Measurements. The tails were cut from the live lizards and reflectance measured by illuminating with an Ocean Optics DH-2000 light source (200 to $2,500\text{ nm}$) and an Ocean Insight FLAME miniature Spectrometer. The light source was coupled in one channel to a THORLABS RP20 reflection probe and the light reflected on the lizard tails at near-normal incidence. The light was collected by the second optical fiber channel to the spectrometer. A white diffuse reflectance standard (Labsphere USRS-99-010, AS-01158-060) was used as a reference. The reflectance spectra were collected from three hatching specimens, two juvenile specimens, and two adult specimens.

Cryo-SEM Imaging. The freshly cut vibratome sections were directly sandwiched between two metal discs (3 mm in diameter, $100\text{ }\mu\text{m}$ in depth each) and then cryoimmobilized in a high-pressure freezing device (LEICA ICE, High-Pressure Freezer). The frozen samples were transferred to a freeze-fracture device (LEICA ACE900 Freeze-Fracture vacuum chamber) by a vacuum cryotransfer sample holder (LEICA VCT500 Cryo-stage) under liquid nitrogen. The samples were freeze-fractured and transferred to a high-resolution GEMINI-300 Zeiss Scanning Electron Microscope. Samples were either imaged directly or after coating with $2\text{-}3\text{ nm}$ of Pt in the ACE900 device. During SEM imaging, the cryo-stage sample holder and the electron microscope were maintained at $-120\text{ }^\circ\text{C}$ by liquid nitrogen. The cryo-SEM images were collected from 12 different hatching sections from three hatching specimens, three different juvenile sections from two juvenile specimens, and four different adult sections from two adult specimens.

Fast Fourier Transform Processing on Cryo-SEM Images. The hatching, juvenile and adult iridophores were randomly selected from cryo-SEM images (13 cells from different areas of three hatching specimens, 13 cells from two juvenile specimens, and 13 cells from different areas of two adult specimens). We estimate that the hatching lizards were between 3 and 5 d post-hatching, and the adult lizards were between 4 and 6 wk post-hatching. The positions and orientations of the crystals in the cryo-SEM images were manually marked by lines, and the resultant images were turned into binary form (*SI Appendix, Fig. S9*). The 2D FFT analysis was conducted on the binarized images using the Directionality plugin in FIJI imageJ (<https://imagej.net/plugins/directionality>, *SI Appendix, Fig. S9*) to determine the preferred orientations of the structure on the binary image (46, 47). For each iridophore cell, the analysis resulted in a probability distribution vs. angle (number of bins, $N = 20$). The entropy (S) of the histogram was calculated according to:

$$S = - \sum_{i=1}^N p_i \ln(p_i),$$

where p_i is the probability in each of N bins (similar to the analysis performed by Bach-Gansmo et al. 48). Then, an unpaired t test was performed to assess whether there is a statistically significant difference between the adult, juvenile, and hatchling lizard groups (the sample size for each group was $n = 13$). The P -value between the adult and juvenile groups was 0.0014, and between the juvenile and hatchling groups was 0.0498. This means that the difference in entropy between the groups was highly significant: 99 and 95%, respectively.

TEM Imaging on Fixed and Stained Ultra-Thin Biological Tissue. The sectioned lizard tails were fixed in 4% paraformaldehyde and 2% glutaraldehyde in 0.1M cacodylate buffer at pH 7.4 (23, 32). The tails were fixed for 12 to 16 h at room temperature and then rinsed four times in cacodylate buffer, then postfixed and stained with 1% osmium tetroxide and 1.5% potassium ferricyanide in 0.1M cacodylate buffer for 1 h. Tissues were then washed four times in cacodylate, dehydrated in increasing concentrations of ethanol, rinsed twice in propylene oxide, infiltrated with increasing concentrations of Agar 100 resin in propylene oxide, and embedded in fresh resin. Ultra-thin (80 nm) cross-sections were cut with a diamond knife on a LKB 3 microtome. The cross-sections were then placed on carbon-formvar-coated copper grids and were poststained with uranyl acetate and lead citrate. TEM imaging on the ultra-thin biological tissues was performed using a Tecnai 12 TEM 100 kV (Phillips) equipped with MegaView II CCD camera. The TEM images were collected from three hatchling specimens and two adult specimens, which include hundreds of cells from hatchling to adult in total.

TEM Imaging and Electron Diffraction of Extracted Guanine Crystals. Crystals were isolated from fixed lizard tail tissues and cleaned in purified water, and a drop of the resulting suspension was placed on a glow-discharged Cu meshed TEM grid and allowed to dry. The resulting samples were observed with a FEI Tecnai T12 G² TWIN TEM operating at 120 kV. Images and electron diffraction patterns were recorded using a Gatan 794 MultiScan CCD camera. The electron diffraction on the sample allows us to determine that the structure of reflecting plates is β -guanine and that individual guanine plates are indeed single crystals.

In Situ Micro Raman Spectroscopy. Fixed lizard tails and the vibratome sections were placed on an Al disc, and the measurements were made using a LabRAM HR Evolution confocal system (Horiba France) with four laser lines (325, 532, 632, and 785 nm) and a modular microscope (BX-FM Olympus) with a 1,024 \times 256-pixel front-illuminated open electrode cooled CCD camera. The confocal microscope had different objectives (LMPPlanFL N 50 \times NA = 0.5, MPlanFL N 100 \times NA = 0.9, and MPlanFL N 150 \times NA = 0.9) that were used as needed. This allowed spectra acquisition (with a spatial resolution of about 1 μm at 100 \times objective) at the iridophore regions (packed with reflecting materials) on the fixed sections. In total, three hatchling sections (from two different hatchling specimens), two juvenile sections (from two different juvenile specimens), and

two adult sections (from one adult specimen) were analyzed. Raman spectra were acquired at 3 to 5 different positions on each section.

Optical Modeling. The scattering cross-section of individual guanine crystals was calculated using the FDTD technique, by integrating over the field scattered by the particle illuminated by a linearly polarized plane wave. The particle was oriented such that the face with the largest area is normal to the direction of propagation of incident light. Reported cross-sections are the average of values obtained with two orthogonal polarizations. Simulations were performed using a commercial-grade electromagnetic solver (50). Reflectance of multilayer stacks was calculated using a 4 \times 4 transfer matrix program. Disorder was introduced as random increments to spacing and thickness, drawn from Gaussian distributions whose width is determined from the variance estimated from cryo-SEM images. The spectra are an average of a hundred trial spectra. In all calculations, the refractive index of guanine was taken to be $n_o = 1.86$ and $n_e = 1.46$, and the spacing between the particles is assumed to possess a refractive index of 1.33 (i.e., cytoplasm). The input parameters (the length, width, and thickness of the crystals at hatchling and adult stages, and the cytoplasm spacing between crystals) were measured and averaged from the cryo-SEM images. For the simulation with disorder shown in Fig. 6B, a total of 420 trials were averaged (0 to 20° angle of incidence with a 1° step; 20 trials with random layer thickness and spacing for each angle of incidence). The images were collected from 12 different hatchling sections from three hatchling specimens and four different adult sections from two adult specimens, which include hundreds of cells in total.

Data, Materials, and Software Availability. All study data are included in the article, *SI Appendix*, and/or the extended Datasets S1–S4.

ACKNOWLEDGMENTS. We thank Profs. Devi Stuart-Fox, Yael Lubin, and Yehu Moran for scientific discussions and advice on the manuscript. This work was supported by an ERC Starting Grant (Grant number: 852948, "CRYSTALEYES") and an Azrieli Foundation Faculty Fellowship awarded to B.A.P. and by Gans Collections and Charitable Fund donation to D.H. B.A.P. is the Nahum Guzik Presidential Recruit. G.Z. is the recipient of the Kreitman Postdoctoral Fellowship. Electron microscopy studies were supported by Ilse Katz Institute for Nanoscale Science & Technology at Ben-Gurion University of the Negev. This work was conducted under Israel Nature and Parks Permits 2020/42592 and 2015/40931.

Author affiliations: ^aDepartment of Chemistry, Ben-Gurion University of the Negev, Be'er Sheva 8410501, Israel; ^bDepartment of Physics of Complex Systems, Weizmann Institute of Science, Rehovot 7610001, Israel; ^cDepartment of Physics, Indian Institute of Technology Kanpur, Kanpur, Uttar Pradesh 208016, India; ^dDepartment of Ecology, Evolution and Behavior, The Hebrew University of Jerusalem, Jerusalem 91904, Israel; ^eDepartment of Philosophy, The Hebrew University of Jerusalem, Jerusalem 9190501, Israel; ^fIlse Katz Institute for Nanoscale Science & Technology, Ben-Gurion University of the Negev, Be'er Sheva 8410501, Israel; ^gChemical Research Support, Weizmann Institute of Science, Rehovot 7610001, Israel; and ^hSchool of Geography, Earth and Atmospheric Sciences, University of Melbourne, Parkville, VIC 3053, Australia

1. C. L. Booth, Evolutionary significance of ontogenetic colour change in animals. *Biol. J. Linn. Soc. Lond.* **40**, 125–163 (1990).
2. D. Wilson, R. Heinsohn, J. A. Endler, The adaptive significance of ontogenetic colour change in a tropical python. *Biol. Lett.* **3**, 40–43 (2007).
3. M. Stevens, Color change, phenotypic plasticity, and camouflage. *Front. Ecol. Evol.* **4**, 51 (2016).
4. M. Lambert, B. Carlson, M. Smylie, L. Swierk, Ontogeny of sexual dichromatism in the explosively breeding wood frog. *Herpetol. Conserv. Biol.* **12**, 447–456 (2017).
5. R. R. Cezário, E. M. Thérézio, A. Marletta, S. N. Gorb, R. Guillermo-Ferreira, Ontogenetic colour change of a sexual ornament in males of a damselfly: Female mimicry, crypsis or both? *Sci. Nat.* **109**, 2 (2021).
6. I. C. Cuthill et al., The biology of color. *Science* **357**, eaan0221 (2017).
7. J. A. Endler, J. Mappes, The current and future state of animal coloration research. *Philos. Trans. R. Soc. Lond. B Biol. Sci.* **372**, 20160352 (2017).
8. G. S. Oxford, R. G. Gillespie, Evolution and ecology of spider coloration. *Annu. Rev. Entomol.* **43**, 619–643 (1998).
9. A. C. Price, C. J. Weadick, J. Shim, F. H. Rodd, Pigments, patterns, and fish behavior. *Zebrafish* **5**, 297–307 (2008).
10. J. K. Valkonen et al., From deception to frankness: Benefits of ontogenetic shift in the anti-predator strategy of alder moth *Acronicta alni* larvae. *Curr. Zool.* **60**, 114–122 (2014).
11. P. A. Todd, W. Qiu, K. Y. Chong, Ontogenetic shifts in carapace patterning and/or colouration in intertidal and subtidal brachyuran crabs. *Raffles Bull. Zool.* **57**, 543–550 (2009).
12. D. Hawlena, R. Boochnik, Z. Abramsky, A. Bouskila, Blue tail and striped body: Why do lizards change their infant costume when growing up? *Behav. Ecol.* **17**, 889–896 (2006).
13. W. E. Cooper Jr., L. J. Vitt, Blue tails and autotomy: Enhancement of predation avoidance in juvenile skinks. *Z. Tierpsychol.* **70**, 265–276 (1985).
14. E. N. Arnold, Caudal autotomy as a defense. *Biol. Reptillia* **16**, 235–273 (1988).
15. A. M. Castilla, G. Alberto, P. Galán, V. Pérez-Mellado, Green tails in lizards of the genus *podarcis*: Do they influence the intensity of predation? *Herpetologica* **55**, 530–537 (1999).
16. P. W. Bateman, P. A. Fleming, To cut a long tail short: A review of lizard caudal autotomy studies carried out over the last 20 years. *J. Zool.* **277**, 1–14 (2009).
17. T. Kuriyama, G. Morimoto, K. Miyaji, M. Hasegawa, Cellular basis of anti-predator adaptation in a lizard with autotomizable blue tail against specific predators with different colour vision. *J. Zool.* **300**, 89–98 (2016).
18. H. C. Sousa et al., Blue tales of a blue-tailed lizard: Ecological correlates of tail autotomy in *Micrablepharus atticolus* (Squamata, Gymnophthalmidae) in a Neotropical savannah. *J. Zool.* **299**, 202–212 (2016).
19. U. O. García-Vázquez, C. J. Pavón-Vázquez, M. Feria-Ortiz, A. N. M. de Oca, A new species of blue-tailed skink (Scincidae: *Plestiodon*) from the Sierra Madre del Sur, Mexico. *Herpetologica* **77**, 85–93 (2021).
20. D. Hawlena, Colorful tails fade when lizards adopt less risky behaviors. *Behav. Ecol. Sociobiol.* **64**, 205–213 (2009).
21. J. T. Bagmar, P. J. Fernandez, R. Fujii, On the blue coloration of vertebrates. *Pigment Cell Res.* **20**, 14–26 (2007).
22. D. Gur, B. A. Palmer, S. Weiner, L. Addadi, Light manipulation by guanine crystals in organisms: Biogenic scatterers, mirrors, multilayer reflectors and photonic crystals. *Adv. Funct. Mater.* **27**, 1603514 (2017).
23. T. Kuriyama, K. Miyaji, M. Sugimoto, M. Hasegawa, Ultrastructure of the dermal chromatophores in a lizard (Scincidae: *Plestiodon latiscutatus*) with conspicuous body and tail coloration. *Zool. Sci.* **23**, 793–799 (2006).
24. T. Kuriyama, A. Murakami, M. Brändley, M. Hasegawa, Blue, black, and stripes: Evolution and development of color production and pattern formation in lizards and snakes. *Front. Ecol. Evol.* **8**, 232 (2020).

25. J.T. Bagnara, J. D. Taylor, M. E. Hadley, The dermal chromatophore unit. *J. Cell Biol.* **38**, 67–79 (1968).
26. J. M. Macedonia, S. James, L. W. Wittle, D. L. Clark, Skin pigments and coloration in the Jamaican radiation of Anolis lizards. *J. Herpetol.* **34**, 99–109 (2000).
27. G. F. Grether, G. R. Kolluru, K. Nersessian, Individual colour patches as multicomponent signals. *Biol. Rev.* **79**, 583–610 (2004).
28. C. A. McLean, A. Lutz, K. J. Rankin, D. Stuart-Fox, A. Moussalli, Revealing the biochemical and genetic basis of color variation in a polymorphic lizard. *Mol. Biol. Evol.* **34**, 1924–1935 (2017).
29. P. Andrade *et al.*, Regulatory changes in pterin and carotenoid genes underlie balanced color polymorphisms in the wall lizard. *Proc. Natl. Acad. Sci. U.S.A.* **116**, 5633–5642 (2019).
30. S. T. Rohrlich, R. W. Rubin, Biochemical characterization of crystals from the dermal iridophores of a chameleon *Anolis carolinensis*. *J. Cell Biol.* **66**, 635–645 (1975).
31. R. L. Morrison, A transmission electron microscopic (TEM) method for determining structural colors reflected by lizard iridophores. *Pigment Cell Res.* **8**, 28–36 (1995).
32. S. V. Saenko, J. Teyssié, D. van der Marel, M. C. Milinkovitch, Precise colocalization of interacting structural and pigmentary elements generates extensive color pattern variation in Phelsuma lizards. *BMC Biol.* **11**, 105 (2013).
33. J. Teyssié, S. V. Saenko, D. van der Marel, M. C. Milinkovitch, Photonic crystals cause active colour change in chameleons. *Nat. Commun.* **6**, 6368 (2015).
34. R. L. Morrison, M. S. Rand, S. K. Frost-Mason, Cellular basis of color differences in three morphs of the lizard *Sceloporus undulatus erythrocephalus*. *Copeia* **1995**, 397–408 (1995).
35. J. Matsumoto, Studies on fine structure and cytochemical properties of erythrophores in swordtail, *Xiphophorus helleri*, with special reference to their pigment granules (Pterinosomes). *J. Cell Biol.* **27**, 493–504 (1965).
36. M. Obika, Formation of pterinosomes and carotenoid granules in xanthophores of the teleost *Oryzias latipes* as revealed by the rapid-freezing and freeze-substitution method. *Cell Tissue Res.* **271**, 81–86 (1993).
37. J. T. Bagnara *et al.*, Common origin of pigment cells. *Science* **203**, 410–415 (1979).
38. S. T. Rohrlich, K. R. Porter, Fine structural observation relating to the production of color by the iridophores of a lizard, *Anolis carolinensis*. *J. Cell Biol.* **53**, 38–52 (1972).
39. R. L. Morrison, S. K. Frost-Mason, Ultrastructural analysis of iridophore organellenogenesis in a lizard, *Sceloporus graciosus* (Reptilia: Phrynosomatidae). *J. Morphol.* **209**, 229–239 (1991).
40. A. Wagner, O. Wen, N. Pinski, B. A. Palmer, Functional molecular crystals in biology. *Isr. J. Chem.* **61**, 668–678 (2021).
41. A. Wagner *et al.*, The non-classical crystallization mechanism of a composite biogenic guanine crystal. *Adv. Mater.* **34**, 2202242 (2022).
42. A. Hirsch *et al.*, "Guanigma": The revised structure of biogenic anhydrous guanine. *Chem. Mater.* **27**, 8289–8297 (2015).
43. A. Hirsch *et al.*, Biologically controlled morphology and twinning in guanine crystals. *Angew. Chem. Int. Ed.* **56**, 9420–9424 (2017).
44. Z. Eyal *et al.*, Plate-like guanine biocrystals form via templated nucleation of crystal leaflets on preassembled scaffolds. *J. Am. Chem. Soc.* **144**, 22440–22445 (2022).
45. A. Wagner *et al.*, Macromolecular sheets direct the morphology and orientation of plate-like biogenic guanine crystals. *Nat. Commun.* **14**, 589 (2023).
46. N. Reznikov, R. Almany-Magal, R. Shahar, S. Weiner, Three-dimensional imaging of collagen fibril organization in rat circumferential lamellar bone using a dual beam electron microscope reveals ordered and disordered sub-lamellar structures. *Bone* **52**, 676–683 (2013).
47. L. F. Deravi *et al.*, Design and fabrication of fibrous nanomaterials using pull spinning. *Macromol. Mater. Eng.* **302**, 1600404 (2017).
48. F. L. Bach-Gansmo *et al.*, Osteocyte lacunar properties in rat cortical bone: Differences between lamellar and central bone. *J. Struct. Biol.* **191**, 59–67 (2015).
49. A. Taflove, S. C. Hagness, M. Piket-May, "Computational electromagnetics: The finite-difference time-domain method" in *The Electrical Engineering Handbook*, W.-K. Chen, Ed. (Academic Press, Burlington, 2005), pp. 629–670.
50. Lumerical, *FDTD: 3D Electromagnetic Simulator* (Lumerical Inc., 2019).
51. R. Ravichandran *et al.*, Functionalised type-I collagen as a hydrogel building block for bio-orthogonal tissue engineering applications. *J. Mater. Chem. B* **4**, 318–326 (2016).
52. M. Xiao, M. D. Shawkey, A. Dhinojwala, Bioinspired melanin-based optically active materials. *Adv. Opt. Mater.* **8**, 2000932 (2020).
53. J. D. Joannopoulos, S. G. Johnson, J. N. Winn, R. D. Meade, *Photonic Crystals: Molding the Flow of Light* (Princeton University Press, ed. 2, 2011).
54. D. Gur *et al.*, Guanine-based photonic crystals in fish scales form from an amorphous precursor. *Angew. Chem. Int. Ed.* **52**, 388–391 (2013).
55. B. A. Palmer, D. Gur, S. Weiner, L. Addadi, D. Oron, The organic crystalline materials of vision: Structure-function considerations from the nanometer to the millimeter scale. *Adv. Mater.* **30**, 1800006 (2018).
56. P. A. D. Wise, M. K. Vickaryous, A. P. Russell, An embryonic staging table for *in ovo* development of *Eublepharis macularius*, the leopard gecko. *Anat. Rec.* **292**, 1198–1212 (2009).
57. T. Kuriyama, M. Hasegawa, Embryonic developmental process governing the conspicuousness of body stripes and blue tail coloration in the lizard *Plestiodon latiscutatus*. *Evol. Dev.* **19**, 29–39 (2017).
58. R. E. Diaz Jr., N. A. Shylo, D. Roellig, M. Bronner, P. A. Trainor, Filling in the phylogenetic gaps: Induction, migration, and differentiation of neural crest cells in a squamate reptile, the veiled chameleon (*Chamaeleo calyptratus*). *Dev. Dyn.* **248**, 709–727 (2019).
59. Z. Lin *et al.*, A staging table of embryonic development for a viviparous (live-bearing) lizard *Eremias multiocellata* (Squamata: Lacertidae). *Reprod. Fertil. Dev.* **33**, 782–797 (2021).
60. H. Durrer, "Colouration" in *Biology of the Integument: 2 Vertebrates*, J. Bereiter-Hahn, A. G. Matoltsy, K. S. Richards, Eds. (Springer Berlin Heidelberg, Berlin, Heidelberg, 1986), pp. 239–247.
61. S. M. Doucet, M. D. Shawkey, G. E. Hill, R. Montgomerie, Iridescent plumage in satin bowerbirds: structure, mechanisms and nanostructural predictors of individual variation in colour. *J. Exp. Biol.* **209**, 380–390 (2006).
62. A. V. Badyaev, E. A. Landeen, Developmental evolution of sexual ornamentation: Model and a test of feather growth and pigmentation. *Integr. Comp. Biol.* **47**, 221–233 (2007).
63. O. D. Onelli *et al.*, Development of structural colour in leaf beetles. *Sci. Rep.* **7**, 1373 (2017).
64. M. J. Henze, O. Lind, B. D. Wilts, A. Kelber, Pterin-pigmented nanospheres create the colours of the polymorphic damselfly *Ischnura elegans*. *J. R. Soc. Interface* **16**, 20180785 (2019).
65. J. Lindström, Early development and fitness in birds and mammals. *Trends Ecol. Evol.* **14**, 343–348 (1999).
66. B. A. Palmer *et al.*, The image-forming mirror in the eye of the scallop. *Science* **358**, 1172–1175 (2017).
67. L. J. Vitt, Tail loss, tail color, and predator escape in *Eumeces* (Lacertilia: Scincidae): Age-specific differences in costs and benefits. *Can. J. Zool.* **64**, 583–592 (1986).
68. R. A. Pyron, F. T. Burbrink, J. J. Wiens, A phylogeny and revised classification of Squamata, including 4161 species of lizards and snakes. *BMC Evol. Biol.* **13**, 93 (2013).
69. E. N. Arnold, Evolutionary aspects of tail shedding in lizards and their relatives. *J. Nat. Hist.* **18**, 127–169 (1984).
70. C. M. Watson, C. E. Roelke, P. N. Pasichnyk, C. L. Cox, The fitness consequences of the autonomous blue tail in lizards: An empirical test of predator response using clay models. *Zoology* **115**, 339–344 (2012).
71. J. P. Huelsenbeck, R. Nielsen, J. P. Bollback, Stochastic mapping of morphological characters. *Syst. Biol.* **52**, 131–158 (2003).
72. L. J. Revell, phytools: An R package for phylogenetic comparative biology (and other things). *Methods Ecol. Evol.* **3**, 217–223 (2012).
73. D. W. Bapst, paleotree: An R package for paleontological and phylogenetic analyses of evolution. *Methods Ecol. Evol.* **3**, 803–807 (2012).